Use of Boundary Control With Second-Order Switching Surface to Reduce the System Order for Deadbeat Controller in Grid-Connected Inverter

Yuanbin He, *Student Member, IEEE*, Henry Shu-Hung Chung, *Senior Member, IEEE*, Carl Ngai-Man Ho, *Senior Member, IEEE*, and Weimin Wu

***Abstract*—Deadbeat control is commonly used in grid-connected inverter with *L* filter, but it faces the challenge of having filter resonance in inverter with *LCL* filter. Although many active damping techniques have been proposed to tackle such phenomenon, their digital implementation would introduce nonminimum phase characteristics. Furthermore, the plant viewed by the deadbeat controller is of high order, making the system performance be susceptible to the drift of the filter parameters. This paper introduces a new perspective of using boundary control with second-order switching surface to reduce the order of the plant viewed by the deadbeat controller. The structure hybridizes the merits of the deadbeat control in its simplicity and the boundary control in achieving wide control bandwidth. Small-signal dynamic modeling of the boundary control is formulated. The performance sensitivities of the overall system to filter parameters and grid inductance variations are studied with the derived models. An online grid inductance estimation algorithm is proposed to assure sufficient phase margin under an extremely weak-grid condition. A 2-kW, 220-V, 50-Hz prototype with the switching frequency of 8 kHz has been built and evaluated. Its steady-state and transient behavior, and harmonic rejection capability under stiff- and weak-grid conditions are discussed.**

***Index Terms*—Boundary control, deadbeat control, inverters, *LCL* filter, second-order switching surface, stiff grid, weak grid.**

NOMENCLATURE

L_1 Filter inductor on the inverter side.
C_f Filter capacitor.
L_2 Filter inductor on the grid side.
L_g Equivalent grid inductance.
u_i Dc-link voltage.
u_C Voltage across C_f.
u_g Voltage at the point of common coupling (PCC).
u_g' Equivalent utility grid voltage.
i_1 Current through L_1.
i_C Current through C_f.
i_g Current injected into the PCC, which is equivalent to the current through L_2.

Manuscript received January 19, 2015; revised April 17, 2015; accepted May 26, 2015. Date of publication June 3, 2015; date of current version November 16, 2015. This work was supported by grants from the Research Grants Council of the Hong Kong Special Administrative Region, China, under Project CityU 112711 and 112512. Recommended for publication by Associate Editor M. Ordonez.

Y. He is with the Centre for Smart Energy Conversion and Utilization Research City, University of Hong Kong, Hong Kong (e-mail: yuanbinhe2-c@my.cityu.edu.hk).

H. S.-H. Chung is with the Centre for Smart Energy Conversion and Utilization Research City, University of Hong Kong, Hong Kong, and also with the Research Institute of Electronic Automation, Shanghai Maritime University, Shanghai 201306, China (e-mail: eeshc@cityu.edu.hk).

C. N.-M. Ho is with the Department of Electrical and Computer Engineering, University of Manitoba, Winnipeg, MB R3T 5V6 Canada (e-mail: carl.ho@umanitoba.ca).

W. Wu is with the Research Institute of Electronic Automation, Shanghai Maritime University, Shanghai 201306, China (e-mail: wmwu@shmtu.edu.cn).

Color versions of one or more of the figures in this paper are available online at http://ieeexplore.ieee.org.

Digital Object Identifier 10.1109/TPEL.2015.2441117

I. INTRODUCTION

AN emerging trend in the electricity industry is a paradigm shift from large power plant to small distributed generation systems located at the point of consumption. Regardless of the type of renewable energy source, grid-connected inverter is a crucial device for converting energy produced by the source to the grid [1], [2]. Its power conversion stage (PCS) mainly consists of a switching network and an output filter. The switching network converts incoming dc power into high-frequency ac power. The output filter allows the line-frequency component to pass and attenuates switching harmonics to the grid. Among various types of filters, third-order inductive-capacitive-inductive (*LCL*) filter has become popular, as it requires smaller reactive components than the classical *L* and *LC* filters [3]. The output current of the filter is programmed by a controller, which generates necessary gate signals to the switches in the switching network.

Among different control techniques, deadbeat control is commonly used in inverters with *L* filter for its simplicity in implementation and its wide control bandwidth. Its control mechanism is illustrated in Fig. 1(a) [4], [5]. However, if the filter is of *LCL* type, deadbeat control would face the challenge of filter resonance [6], as the filter has a high quality factor at the resonant frequency. In [7] and [8], an active damping functional block is integrated into the deadbeat control to alleviate such filter resonance. A typical structure is shown in Fig. 1(b). Since the plant controlled by the deadbeat controller is of high order, the system performance would be sensitive to filter parameters and grid impedance variations [8]. Such parametric sensitivity would increase in the digitized system having sampling and computational delay [9], [10], which would introduce nonminimum phase characteristics and lessen the overall stability margin. To mitigate such effect, the circuit variable (e.g., capacitor current) used in the active-damping functional block can be sampled by either shifting the sampling instants [11], [12] or using multisampling technique [13]. However, both of

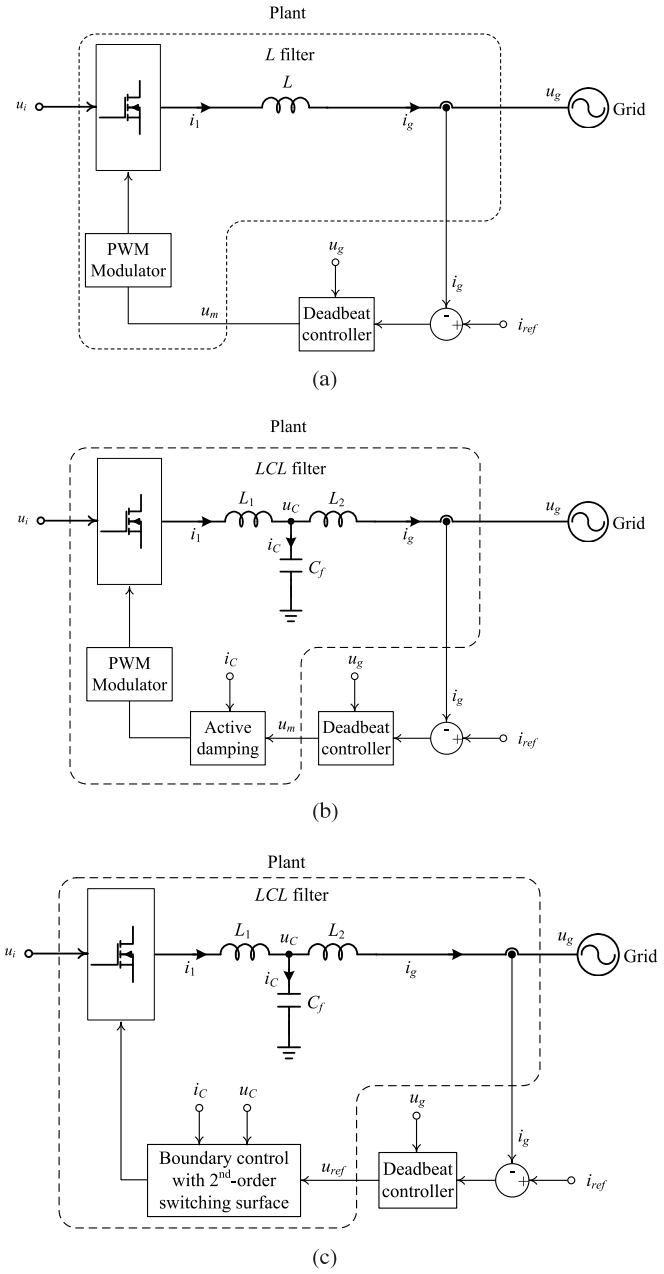

Fig. 1. Comparison of various control methods for inverter with deadbeat control. (a) Deadbeat control for inverter with an *L* Filter. (b) Deadbeat control with active damping for inverter with an *LCL* filter. (c) Proposed method.

them would be susceptible to aliasing error. In [14], the variable used for active damping is estimated by an observer, but the performance is affected by the parameter drift.

A new perspective of using the boundary control with second-order switching surface [15] to reduce the order of the plant viewed by the deadbeat controller is presented. The boundary control determines appropriate switching instants so as to make the system achieve fast dynamic response [15]. The basic structure of the proposed configuration is shown in Fig. 1(c). It hybridizes the merits of the deadbeat control and the boundary control, and offers good grid disturbance rejection capability. The system configuration will be described in Section II. The large-signal stability of the boundary control, and the small-signal ac models for the boundary control and the overall system will be analyzed in Section III. The performance sensitivities to filter parameters and grid inductance variations will be studied with the derived models. An online grid inductance estimation algorithm will be proposed to assure sufficient phase margin under an extremely weak-grid condition in Section IV. A 2-kW, 220-V, 50-Hz prototype with switching frequency of 8 kHz has been built and evaluated. Its steady-state and transient behavior, and harmonic rejection capability under the stiff- and weak-grid conditions are discussed in Section V. The conclusion follows in Section VI.

II. System Configuration

The structure of the grid-connected inverter is shown in Fig. 2. It consists of two main parts, including the PCS and the proposed controller. The PCS consists of a switching network formed by the switches $S_1 \sim S_4$, and an *LCL* filter formed by the inductor L_1, capacitor C_f, and inductor L_2. r_1, r_f, and r_2 are the equivalent series resistances of L_1 and L_2, respectively. L_g and R_g are the equivalent grid inductance and resistance. In the following analysis, R_g is ignored so as to simulate the worst-case condition, where no resistive damping appears on the grid side.

A. State-Space Representation of the PCS

The state-space equations for describing the operation of the PCS are

$$\dot{x} = Ax + Bu_i + Cu_g \tag{1}$$

where $x = [i_1 \ i_g \ u_C]$ and matrices A, B, and C are defined as

$$A = \begin{bmatrix} -(r_1 + r_f)/L_1 & r_f/L_1 & -1/L_1 \\ r_f/L_2 & -(r_2 + r_f)/L_2 & 1/L_2 \\ 1/C_f & -1/C_f & 0 \end{bmatrix}$$

$$B = \begin{bmatrix} q/L_1 \\ 0 \\ 0 \end{bmatrix}, \ C = \begin{bmatrix} 0 \\ -1/L_2 \\ 0 \end{bmatrix}$$

and q is the state of the switching network.

The switching network can be operated in either unipolar pulse-width modulation or bipolar pulse-width modulation (BPWM) [16], [20]. For the sake of simplicity in the analysis, the BPWM is adopted. The output voltage of the switching network is either u_i or $-u_i$, depending on the states of $S_1 \sim S_4$. The switching network has two operating modes: Mode 1 and Mode 2. In the Mode-1 operation, (S_1, S_4) are on and (S_2, S_3) are off. Then, $q = 1$ in (1). In the Mode-2 operation, (S_1, S_4) are off and (S_2, S_3) are on. Then, $q = -1$ in (1). Considering that the switching frequency of the switching network is much higher than the line frequency, i_g is fairly constant over the switching period and the switching current ripple through C_f is

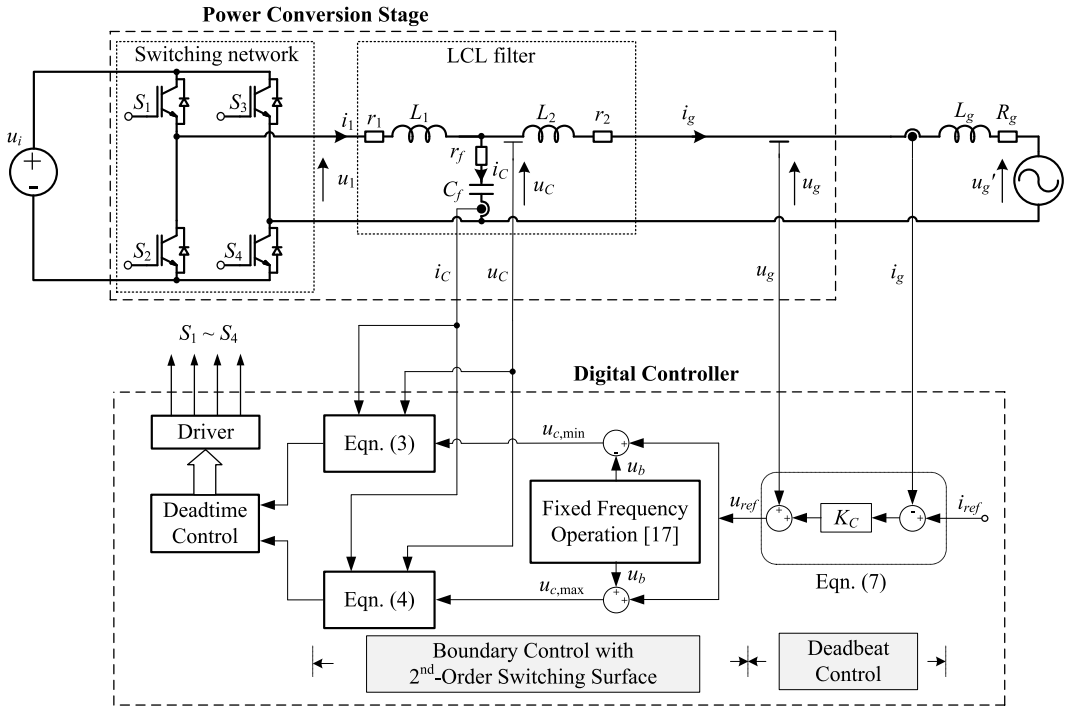

Fig. 2. Architecture of the inverter with the proposed control scheme.

nearly the same as that through L_1. (1) can be simplified into

$$\begin{bmatrix} di_C/dt \\ du_C/dt \end{bmatrix} \cong \begin{bmatrix} di_1/dt \\ du_C/dt \end{bmatrix} = \begin{bmatrix} -(r_1+r_f)/L_1 & -1/L_1 \\ 1/C_f & 0 \end{bmatrix} \begin{bmatrix} i_C \\ u_C \end{bmatrix} + \begin{bmatrix} q/L_1 \\ 0 \end{bmatrix} u_i + \begin{bmatrix} -r_1/L_1 \\ 0 \end{bmatrix} i_g. \quad (2)$$

B. Derivation of the Control Law

The proposed controller consists of two control loops. The outer loop is used to regulate the grid current i_g by using a deadbeat controller. It generates a filter-capacitor voltage reference $u_{\rm ref}$ for the inner loop. The inner loop is used to regulate the voltage across C_f, u_C, at $u_{\rm ref}$ by using the boundary control with second-order switching surface to dictate the switching instants.

In the boundary control, the switching criterion for the Mode-1 operation is

$$u_C(t) \le u_{C,\min}(t) + K_1(t)\left[i_C^2(t) - I_{C,line}^2(t)\right] \quad (3)$$

and the switching criterion for the Mode-2 operation is

$$u_C(t) \ge u_{C,\max}(t) + K_2(t)\left[i_C^2(t) - I_{C,\rm line}^2(t)\right] \quad (4)$$

where $I_{C,\rm line}$ is the line-frequency component of the current through C_f.

Detailed derivations of (3) and (4) are given in Appendix A.

In Fig. 2, a filter capacitor voltage reference $u_{\rm ref}$ is generated by the deadbeat controller. Then, a variable band u_b is added onto $u_{\rm ref}$ to generate $u_{C,\min}$ and $u_{C,\max}$.

$$u_{C,\min}(t) = u_{\rm ref}(t) - u_b(t) \quad (5)$$

$$u_{C,\max}(t) = u_{\rm ref}(t) + u_b(t). \quad (6)$$

Thus, (3) and (4) are used to derive the gate signals for the switches. The switching frequency of the switches is regulated at the designed value through a simple feedback mechanism described in [17]. The difference between the actual switching period and reference switching period is amplified and is used to generate u_b.

Based on [18], the deadbeat current control law for the system is

$$\begin{aligned} u_{\rm ref}[k] &= K_C\{i_{\rm ref}[k] - i_g[k]\} + r_2\, i_g[k] + u_g[k] \\ &\cong K_C\{i_{\rm ref}[k] - i_g[k]\} + u_g[k]. \end{aligned} \quad (7)$$

where $i_{ref}[k], i_g[k], u_{\rm ref}[k]$, and $u_g[k]$ are the kth sampled values of $i_{\rm ref}$, i_g, $u_{\rm ref}$, and u_g, respectively.

K_C is the deadbeat current control gain and given as

$$K_C = \frac{L_2}{T_{\rm samp}}\Big|_{L_2 = L_{2,N}} \quad (8)$$

where $T_{\rm samp}$ is the sampling period and $L_{2,N}$ is the nominal value of L_2.

III. System Modeling and Parametric Sensitivities

As demonstrated in [19], the boundary control with second-order switching surface outperforms the hysteresis and sliding-mode control in achieving fast dynamic response. Its stability analysis is mainly based on time-domain modeling [19]–[21]. As the boundary control performs fast response, it is usually approximated as a unity gain in the overall control [22]. Less emphasis is placed on its frequency response. As will be conducted in the following analysis, the boundary control block

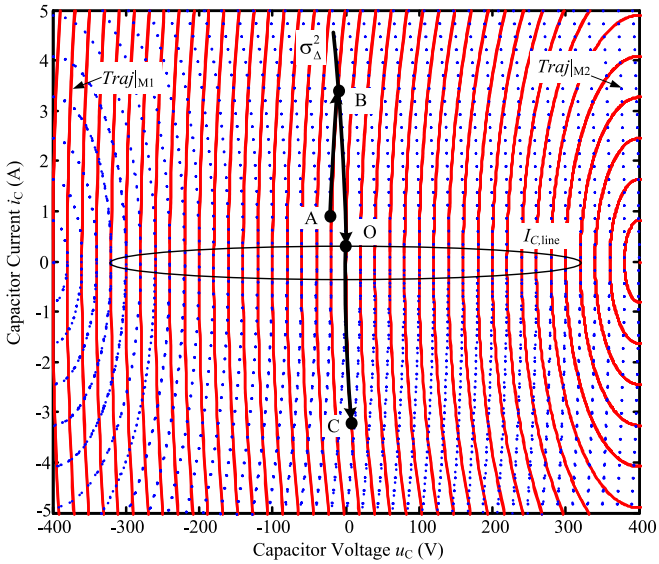

Fig. 3. $i_C - u_C$ plane.

combined with the output filter will reduce the system order viewed and controlled by the deadbeat controller. Even if the actual output filter is of *LCL* type, the deadbeat controller operates with a plant, like an *L*-filter system.

In this section, the large-signal characteristics of the boundary control with second-order switching surface will be first discussed. Then, the small-signal ac model of the boundary control will be derived and integrated into the whole system together with the deadbeat controller. The derived model will be also used to study the performance sensitivities to parameter variations.

A. Large-Signal Characteristics of the Boundary Control

Based on (A5) and (A6) in Appendix A, the approximated Mode-1 trajectory $\mathrm{Traj}|_{\mathrm{M1}}$ and Mode-2 trajectory $\mathrm{Traj}|_{\mathrm{M2}}$ can be expressed respectively

$$\mathrm{Traj}|_{\mathrm{M1}} = u_C(t) - u_C(t_2) - K_{S1}(t)\left[i_C^2(t) - i_C^2(t_2)\right] = 0 \tag{9}$$

$$\mathrm{Traj}|_{\mathrm{M2}} = u_C(t) - u_C(t_4) - K_{S2}(t)\left[i_C^2(t) - i_C^2(t_4)\right] = 0 \tag{10}$$

where $K_{S1}(t) = \frac{L_1}{2C_f[u_i - u_C(t)]}$ and $K_{S2}(t) = \frac{-L_1}{2C_f[u_i + u_C(t)]}$ are the trajectory parameters during Mode-1 and Mode-2 trajectories, respectively. The filter parameters in $K_{S1}(t)$ and $K_{S2}(t)$ are the actual values.

By solving (9) and (10) with different initial conditions, families of $\mathrm{Traj}|_{\mathrm{M1}}$ and $\mathrm{Traj}|_{\mathrm{M2}}$ on the $i_C - u_C$ state plane are given in Fig. 3, where $\mathrm{Traj}|_{\mathrm{M1}}$ are drawn with red solid lines while $\mathrm{Traj}|_{\mathrm{M2}}$ are drawn with blue dotted lines. The tangential component of the trajectory velocity along the switching surface determines the rate at which successor points approach or recede from the equilibrium point (i.e., "O"). Depending on the location of the initial state, for example, either state "A" or "B," switching criteria based on second-order surfaces σ^2_Δ, which is along either the only Mode-1 state trajectory or Mode-2 state trajectory, are derived. The ultimate objective is to make the system reach the equilibrium point "O" in two switching actions.

To analyze the stability, the switching criteria are rewritten as a second-order switching surface σ^2_Δ

$$\begin{cases} \sigma^2_{\Delta-} = u_C(t) - u_{\mathrm{ref}}(t) - K_1(t)\left[i_C^2(t) - I_{C,line}^2(t)\right] \\ \qquad\quad + u_b(t) \quad (i_C(t) < 0) \\ \sigma^2_{\Delta+} = u_C(t) - u_{\mathrm{ref}}(t) - K_2(t)\left[i_C^2(t) - I_{C,line}^2(t)\right] \\ \qquad\quad - u_b(t) \quad (i_C(t) > 0) \end{cases} \tag{11}$$

where $K_1(t) = \frac{L_{1,N}}{2C_{f,N}[u_i - u_C(t)]}$ and $K_2(t) = \frac{-L_{1,N}}{2C_{f,N}[u_i + u_C(t)]}$ are the control parameters during Mode-1 and Mode-2 operations. $K_1(t)$ and $K_2(t)$ are calculated with the nominal values $L_{1,N}$ and $C_{f,N}$ for L_1 and C_f, respectively. However, the actual values of L_1 and C_f expressed in (9) and (10) should have variations, due to factors such as component tolerance, temperature effect, aging effect, etc.

By varying the control parameters $K_1(t)$ and $K_2(t)$, the points along $\sigma^2_\Delta = 0$ are divided based on the directions of trajectories at the switching surface [23]. Thus, there are three possible modes of the points: rejective mode, reflective mode and refractive mode. In rejective mode, the points depart away from the switching surface on both sides, which will lead to unstable operation of the inverter. In reflective mode, the points direct toward the switching surface on both sides and lead to stable operation. In refractive mode, the points direct toward the switching surface on one side and away it on the other side, where the state moves around the target operating surface. As derived in Appendix B, the regions of the control parameters, $K_1(t)$ and $K_2(t)$, for the three modes are as follows:

Rejective mode

$$K_1(t) < K_{S2}(t) \text{ and } K_2(t) > K_{S1}(t). \tag{12}$$

Reflective mode

$$K_1(t) > K_{S1}(t) \text{ and } K_2(t) < K_{S2}(t). \tag{13}$$

Refractive mode

$$K_{S2}(t) < K_1(t) < K_{S1}(t) \text{ or} \tag{14a}$$

$$K_1(t) > K_{S1}(t) \text{ and } K_2(t) > K_{S2}(t) \text{ or} \tag{14b}$$

$$K_1(t) < K_{S2}(t) \text{ and } K_2(t) < K_{S1}(t) \tag{14c}$$

where the condition for stable operation in refractive mode is calculated as

$$K_1(t) > K_2(t). \tag{15}$$

Thus, Fig. 4 shows the regions for different modes under different combinations of $K_1(t)$ and $K_2(t)$. When $K_1(t) = K_{S1}(t)$ and $K_2(t) = K_{S2}(t)$, the switching surface is along the boundary of the reflective and refractive regions.

Based on the equations for trajectory parameters and control parameters presented in (9)–(11), the following relationships

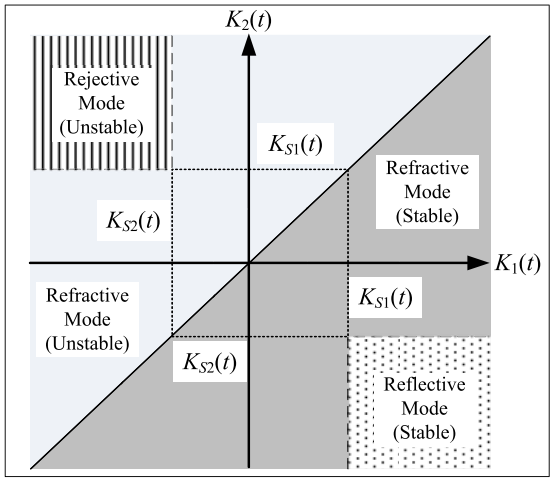

Fig. 4. Stability analysis of the boundary control with different $K_1(t)$ and $K_2(t)$.

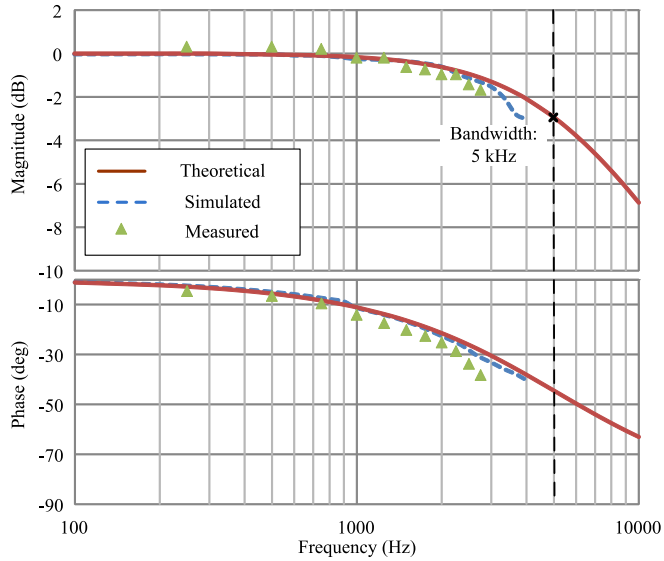

Fig. 5. Theoretical, simulated, and measured frequency characteristics of $G_{BC}(s)$.

are always met:

$$K_1(t) > K_{S2}(t) \tag{16a}$$

$$K_2(t) < K_{S1}(t) \tag{16b}$$

$$K_1(t) > K_2(t). \tag{16c}$$

Thus, by combining (12)–(16), there are only two possible operation modes for the BPWM regulated inverter. They are reflective and refractive modes with stable operation, ensuring large-signal stability.

B. Small-Signal AC Model of the Boundary Control

Assume that there is no dead time from the command generated by the digital controller to the gate of the switches. At the switching instants t_1 and t_3 in Fig. 22

$$u_C(t_1) = u_{C,\min}(t_1) + K_1(t_1)\left[i_C^2(t_1) - I_{C,line}^2(t_1)\right] \tag{17}$$

and

$$u_C(t_3) = u_{C,max}(t_3) + K_2(t_3)\left[i_C^2(t_3) - I_{C,\text{line}}^2(t_3)\right] \tag{18}$$

where $K_1(t_1)$ and $K_2(t_3)$ are calculated with the nominal values $L_{1,N}$ and $C_{f,N}$ for L_1 and C_f, respectively. They can be expressed as

$$L_1 = L_{1,N}(1 + \alpha) \tag{19}$$

$$C_f = C_{f,N}(1 + \beta) \tag{20}$$

where α and β are the tolerances of L_1 and C_f, respectively.

Then, the closed-loop transfer function of the boundary control operating at a fixed switching frequency, $G_{\text{BC}}(s)$, is

$$G_{BC}(s) = \frac{\Delta U_{\text{C}}(s)}{\Delta U_{\text{ref}}(s)} = \frac{1}{s\frac{T_S(1+\beta)}{4(1+\alpha)} + 1}. \tag{21}$$

Detailed derivation of (21) is given in Appendix C.

Thus, the boundary control can make the transfer characteristics from u_{ref} to u_C in Figs. 1(c) and 2 become a first-order system with an equivalent time constant T_{BC}, where

$$T_{BC} = \frac{T_S}{4}\frac{(1 + \beta)}{(1 + \alpha)}. \tag{22}$$

The above analysis elucidates the small-signal dynamical properties of the system with the boundary control with second-order switching surface. It gives a new perspective the performance characteristics in frequency domain. The key merit, as compared with the classical time-domain methods [19]–[21], is that the derived transfer function can be integrated into system modeling, design, and analysis with the rest of the functional blocks in the system. Based on the expression of $G_{\text{BC}}(s)$, the following points are noted:

1) In the classical cascade control method with fast inner loop and slow outer loop [24], the fast inner loop does not reduce the system order for the outer loop. However, in the proposed method, after combining the fast boundary control loop with the output filter, the system order for the outer deadbeat control loop is reduced.
2) The parameters used in the control law are well defined and determined by the filter parameters.

Fig. 5 shows the theoretical, simulated, and measured frequency response curves of $G_{\text{BC}}(s)$. The parameters used are all nominal values. The simulated curve is based on the results obtained by PSIM. The results are all in close agreement.

C. Dynamical Modeling of the System

Fig. 6(a) shows the block diagram of the whole system with the inner boundary control and outer deadbeat control. The ac grid current $\Delta I_g(s)$ can be expressed as

$$\Delta I_g(s) = G_{ii}(s)\,\Delta I_{\text{ref}}(s) + G_{\text{iv}}(s)\,\Delta U_g'(s) \tag{23}$$

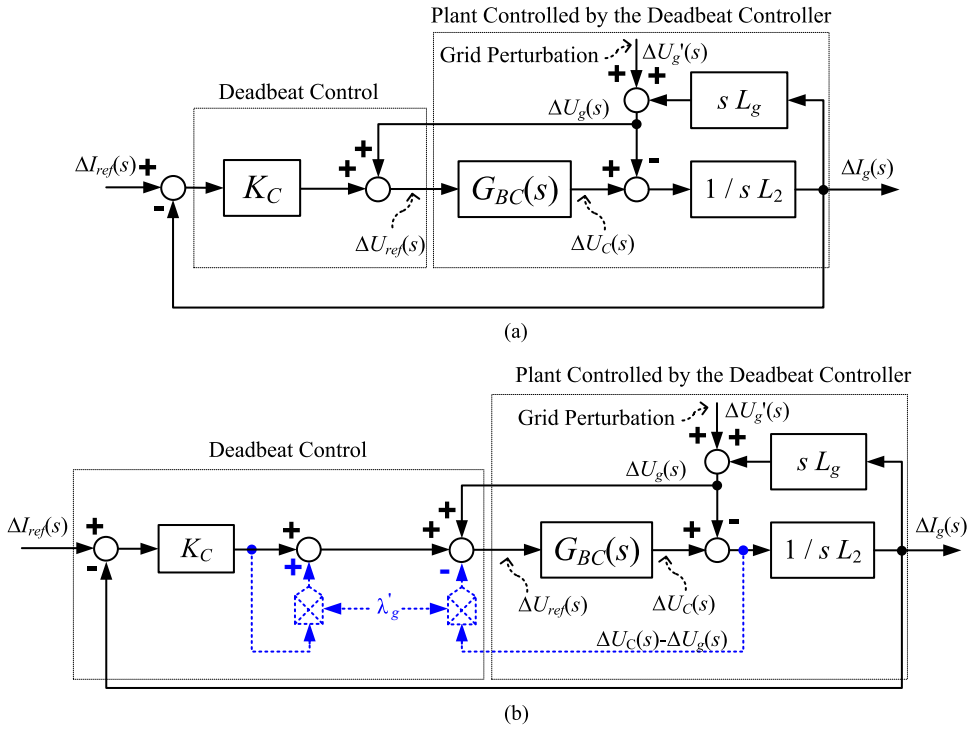

Fig. 6. Block diagrams of the control scheme. (a) Without grid inductance estimation. (b) With grid inductance estimation.

where

$$G_{ii}(s) = \frac{K_C G_{BC}(s)}{s\left[L_2 + L_g - L_g G_{BC}(s)\right] + K_C G_{BC}(s)} = \frac{1}{s^2 \frac{T_S^2}{4\Psi}\frac{(1+\beta)(1+\gamma)(1+\lambda_g)}{1+\alpha} + s\frac{T_S}{\Psi}(1+\gamma)+1} \quad (24)$$

and

$$G_{iv}(s) = \frac{G_{BC}(s) - 1}{s\left[L_2 + L_g - L_g G_{BC}(s)\right] + K_C G_{BC}(s)} = -\frac{s\frac{T_S^2}{4\Psi L_{2,N}}\frac{1+\beta}{1+\alpha}}{s^2 \frac{T_S^2}{4\Psi}\frac{(1+\beta)(1+\gamma)(1+\lambda_g)}{1+\alpha} + s\frac{T_S}{\Psi}(1+\gamma)+1} \quad (25)$$

where $L_2 = L_{2,N}\,(1+\gamma)$, $\lambda_g = L_g \,/\, L_2$, and $T_{\text{samp}} = \Psi\, T_S$.

In the above expressions, γ is the tolerance of L_2, λ_g is the ratio between L_g and L_2, and Ψ is the ratio between the sampling frequency and the switching frequency. Based on (23), the grid current is determined by two input variables: current reference i_{ref} and grid voltage u_g' (see Fig. 2). $G_{ii}(s)$ is the reference-current-to-output-current transfer function, describing the transfer characteristics from the reference current i_{ref} to the grid current i_g. $G_{iv}(s)$ is the grid-voltage-to-grid-current transfer function, measuring the susceptibility of the grid current to the grid voltage.

Based on (24) and (25), $G_{ii}(s)$ and $G_{iv}(s)$ are functions of the filter parameters and the grid inductance L_g. Variations of the parameters on affecting the performance characteristics of $G_{ii}(s)$ and $G_{iv}(s)$ are discussed below.

1) Characteristics of $G_{ii}(s)$ Against Parameter Variations: The loop gain of $G_{ii}(s)$, $G_{O,ii}(s)$, is

$$G_{O,ii}(s) = \frac{1}{s^2 \frac{T_S^2}{4\Psi}\frac{(1+\beta)(1+\gamma)(1+\lambda_g)}{1+\alpha} + s\frac{T_S}{\Psi}(1+\gamma)}. \quad (26)$$

The crossover frequency ω_{PM} is calculated by solving (26) with $|G_{O,ii}(j\omega_{PM})| = 1$

$$\omega_{PM} = \frac{4(1+\alpha)}{T_S(1+\beta)(1+\lambda_g)} \sqrt{\frac{\sqrt{1+\left[\frac{\Psi}{2}\frac{(1+\beta)(1+\lambda_g)}{(1+\alpha)(1+\gamma)}\right]^2}-1}{2}}. \quad (27)$$

Thus, the phase margin PM is

$$PM = 180^\circ + \angle G_{O,ii}(\omega_{PM}) = 90^\circ - \frac{180^\circ}{\pi}\tan^{-1}\sqrt{\frac{\sqrt{1+\left[\frac{\Psi}{2}\frac{(1+\beta)(1+\lambda_g)}{(1+\alpha)(1+\gamma)}\right]^2}-1}{2}}. \quad (28)$$

(28) reveals that positive drift of C_f (i.e., β is positive), negative drift of L_1 (i.e., α is negative) and L_2 (i.e., γ is negative), and increase of the equivalent grid inductance (i.e., λ_g is positive) will reduce the phase margin.

As the typical component tolerance is within 20%, the worst-case condition with $\alpha = \gamma = -0.2$ and $\beta = +0.2$ is considered. Based on that, the system performance under a wide variation of grid inductance is studied, i.e., λ_g varies from zero to 6.4 (640%). Fig. 7(a) and (b) shows the phase margin *PM* and the crossover

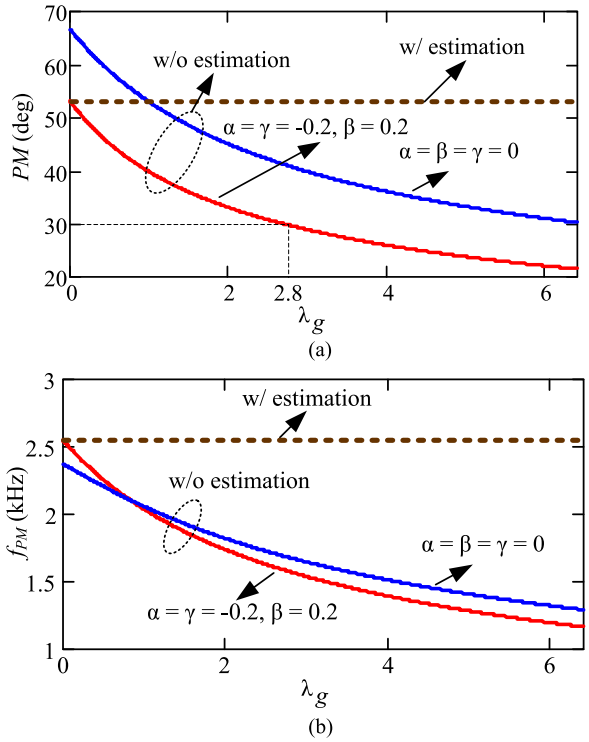

Fig. 7. System performance versus grid inductance. (a) Phase margin. (b) Crossover frequency.

TABLE I
VALUES OF THE COMPONENTS USED IN THE INVERTER PROTOTYPE

	System Parameter	Value (p.u.∗)
LCL filter	L_1	3.6 mH (0.047 p.u.)
	L_2	1.2 mH (0.016 p.u.)
	C_f	6 μF (0.046 p.u.)
Grid impedance (inductive)	Minimum value L_g	0.1 mH (0.0013 p.u.)
	Maximum value L_g (weak grid)	7.7 mH (0.10 p.u.)
Switching frequency	f_S	8 kHz
Dc link voltage	u_i	405 V
Grid voltage	u'_g	220 V
Grid frequency	f	50 Hz
Rated power	P_{rated}	2000 W

∗Base value for calculating the per unit (p.u.) is u_g^2 / P_{rated}.

frequency ω_{PM} versus the value of λ_g at $\Psi = 2$. As λ_g increases significantly, the phase margin can still be maintained above 30° under nominal filter parameters. However, with significant filter parameters drift, the phase margin will decrease below 30° when $\lambda_g > 2.8$, while the crossover frequency f_{PM} is maintained over 1 kHz.

Based on the given parameters in Table I, the frequency plots of the loop gain with different grid inductances are shown in Fig. 8, where the maximum achievable crossover frequency is 2.6 kHz. By comparing the bandwidth of the boundary control shown in Fig. 5 (i.e., 5 kHz), the separation of the dynamic response between the internal and external loops is not evident. Such phenomenon is different from the classical cascade control with evident separation of bandwidths of the inner and outer control loops [24]. It is because the dynamic response of

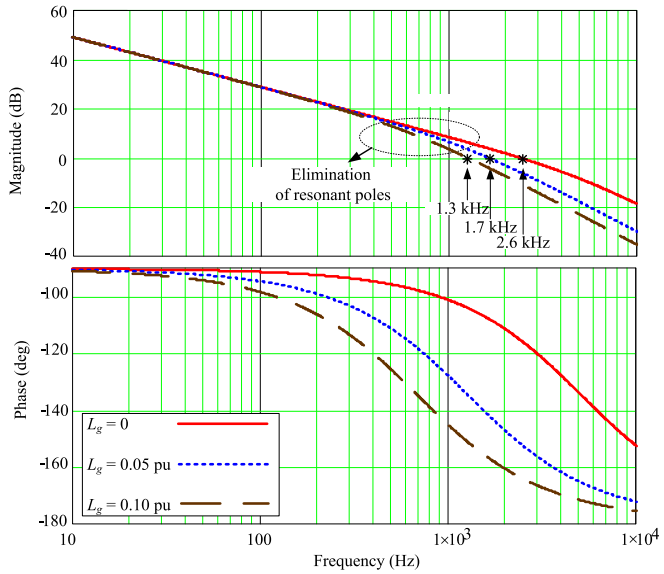

Fig. 8. Frequency plots of $G_{O,ii}(s)$ with different grid inductances.

the outer loop has to be fast, so as to ensure fast grid current tracking. As shown in Fig. 8, the entire system operates with adequate stable margin and fast grid current tracking ability. More importantly, by adopting the proposed architecture, wide control bandwidth is guaranteed under the extremely weak-grid condition.

2) Characteristics of $G_{iv}(s)$ Against Parameter Variations: The reciprocal of the transfer function $G_{iv}(s)$ can be considered as the input impedance. In order to attenuate the effect of the harmonic component in u'_g on the grid current, the magnitude of $G_{iv}(s)$ should be kept small. In other words, the input impedance $Z_{in}(s) = 1/|G_{iv}(s)|$ should be kept large. In the proposed control structure, the input impedance is mainly guaranteed by the feedforward term of terminal voltage u_g in the deadbeat controller, which is adaptive to the grid frequency variation [25]. By substituting (21) into (25), the magnitude of $Z_{in}(s)$ can be shown to be

$$Z_{in}(j\omega) = \omega\, L_{2,N} \sqrt{\left[\frac{4\Psi}{\omega^2 T_S^2}\frac{1+\alpha}{1+\beta} - (1+\gamma)(1+\lambda_g)\right]^2 + \left(\frac{4}{\omega T_S}\frac{(1+\alpha)(1+\gamma)}{1+\beta}\right)^2}. \tag{29}$$

The input impedance is capacitive at low frequency and becomes inductive at high frequency. Such phenomenon can be explained by considering that the inverter can be modeled as a current source with parallel output capacitive impedance connecting to the grid through series inductive impedance. Thus, the low-frequency impedance is capacitive and the high-frequency impedance is inductive. A detailed discussion on modeling the input impedance of grid-connected inverter is given in [26].

Again, keeping $\alpha = \gamma = -0.2$ and $\beta = +0.2$, the frequency characteristics of the input impedance are analyzed under different grid inductances. Based on the parameters in Table I, Fig. 9 shows $Z_{\text{in}}(j\omega)$ against different grid inductance, at $\Psi = 2$. As

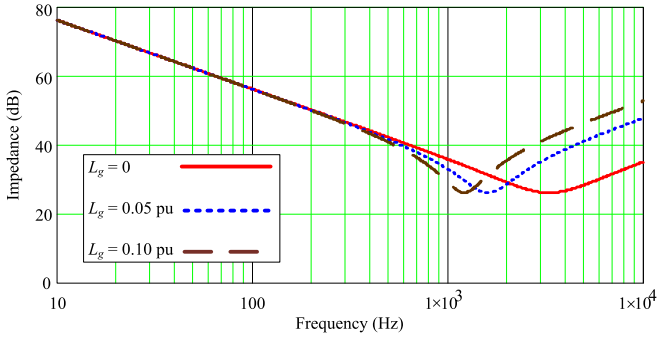

Fig. 9. Input impedance under different grid inductances.

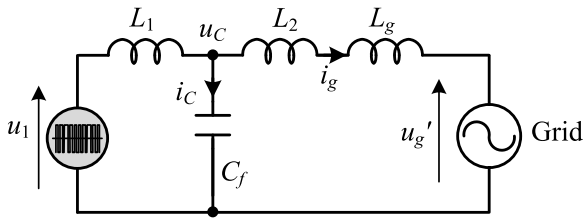

Fig. 10. Simplified equivalent circuit of the system.

L_g increases, the grid-side input impedance of the inverter will reduce within a frequency range. As shown in Fig. 9, the input impedance with $L_g = 0.10$ p.u. is slightly smaller than that with $L_g = 0$ between the frequency of 350 Hz and 1.5 kHz.

Based on the observations, the phase margin and input impedance can be improved if the value of L_g (and thus λ_g) can be determined and be used to modify the control law. Thus, a simple online grid inductance algorithm will be proposed in the next section.

IV. Online Grid Inductance Algorithm

There are many reported passive and active methods for estimating the grid impedance. The passive techniques are mainly based on utilizing the disturbances already present in the power networks, e.g., the fundamental- or low-order harmonic frequencies [27], [28]. The active techniques are based on injecting disturbance into the grid impedance at individual frequencies or in characteristic frequency bands [29]–[32]. As the performance of passive methods is susceptible to the level of the inherent disturbances, the active approaches with tunable disturbances are more popular. However, the injected disturbances would deteriorate the power quality at the PCCs. In order to mitigate the problem, the inherent switching information in the circuit is used to estimate the equivalent grid inductance. The algorithm is realized by using a simple feedback mechanism.

Fig. 10 shows the simplified equivalent circuit of the PCS. The switching circuit generates both line-frequency component and high-frequency switching harmonics, while the grid voltage u_g' is of low frequency. By using the Kirchhoff's voltage law

$$\frac{1}{C_f}\int i_C\,dt = u_C = u_{L2} + u_{Lg} + u_g' \tag{30}$$

where u_{L2} and u_{Lg} are the voltages across L_2 and L_g, separately.

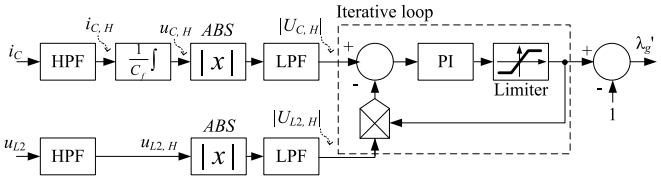

Fig. 11. Online grid inductance estimation algorithm.

By considering the switching-frequency components

$$\frac{1}{C_f}\int i_{C,H}\,dt = u_{C,H} = u_{L2,H} + u_{Lg,H} = (\lambda_g + 1)u_{L2,H} \tag{31}$$

where $i_{C,H}$, $u_{C,H}$, $u_{L2,H}$, and $u_{Lg,H}$ are the switching-frequency components of i_C, u_C, u_{L2}, and u_{Lg}, respectively.

A. Implementation of the Algorithm

Based on (31), $u_{C,H}$ can be determined by integrating $i_{C,H}$. As the resolution of the switching-frequency component of i_C is higher than that of u_C practically. The value of L_g is estimated by first calculating λ_g. Again, by using (31)

$$\lambda_g = \frac{u_{C,H}}{u_{L2,H}} - 1 \tag{32}$$

where $u_{C,H}$ and $u_{L2,H}$ have the same harmonic content based on the equivalent circuit in Fig. 10. Thus, in the practical implementation, instead of using the real-time values of $u_{C,H}$ and $u_{L2,H}$ to calculate λ_g, (32) is modified by using their low-frequency rectified values as

$$\lambda_g = \frac{\frac{1}{C_f}\,\mathrm{LPF}[\mathrm{ABS}(\int i_{C,H}\,dt)]}{\mathrm{LPF}[\mathrm{ABS}(u_{L2,H})]} - 1 \tag{33}$$

where LPF and ABS represent the first-order low-pass filter (LPF) and the absolute value, respectively.

Fig. 11 shows the feedback mechanism for determining the estimated value of λ_g, λ_g', where the plant controlled by the proportional-integral (PI) functional block in the iterative loop is viewed as a unity gain and the stability of the iterative loop is determined by the block. $i_{C,H}$ and $u_{L2,H}$ are obtained by two high-pass filters (HPFs). The outputs are rectified and their low-frequency components are obtained by using two LPFs. The bandwidth selection of the LPFs should be much wider (i.e., over ten times) than that of the iterative loop in Fig. 11. Then, λ_g' is iterated by using the feedback loop, in which the value of λ_g' is updated by using equation (33).

Based on Fig. 2, i_C and u_C are sampled for the boundary control. The inductor voltage u_{L2} can be obtained readily by using the equation of

$$u_{L2} = u_C - u_g. \tag{34}$$

Thus, the grid inductance estimation is based on the sampled data for the control system. Fig. 12(a) shows the comparison among the actual grid inductance, simulation result, and estimated grid inductance calculated by the controller in the prototype in Section V, where the initial grid inductance is set at 2.4 mH and it is suddenly changed to 1.8 mH after one second. The

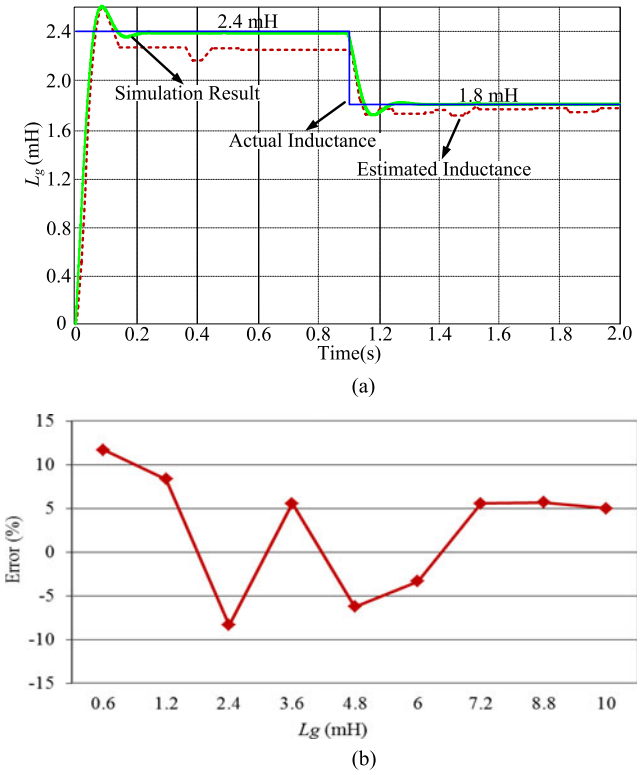

Fig. 12. Performance of the online grid inductance estimation algorithm. (a) Time-domain results. (b) Accuracy.

algorithm can respond to such change in less than 0.2 s. Due to the impact of aliasing error, the estimated grid inductance may vary during steady state in Fig. 12(a). Fig. 12(b) shows the error of the estimation together with experimental validation. It is found that the error is within $\pm 15\%$, being close to prior methods in [28] and [29].

With the estimated grid inductance, the deadbeat control is modified as shown in Fig. 6(b), in which the gain K_C is redesigned to maintain the system bandwidth and a feedback path taken from u_{L2} is introduced to mimic the grid voltage (i.e., u_g') feedforward for decoupling the effect of L_g totally. The modified gain K_C' is

$$K_C' = \frac{(1+\lambda_g')L_{2,N}}{T_{\text{samp}}} = (1+\lambda_g')\,K_C. \tag{35}$$

Thus, $G_{O,ii}(s)$ is modified with the new gain as follows:

$$G_{O,ii}'(s) = \frac{K_C}{sL_2\left[s\frac{T_S(1+\beta)}{4(1+\alpha)}\left(\frac{1+\lambda_g}{1+\lambda_g'}\right)+1\right]}. \tag{36}$$

Therefore, based on the analysis in Section III, the system performs well at $\lambda_g' = \lambda_g$ because the influence of the equivalent grid inductance on the inverter output current is decoupled. Based on (26), Fig. 7 shows that the crossover frequency and phase margin are both significantly improved with accurate grid inductance estimation.

B. Impact of the Deviation on System Performance

Considering that there is deviation in determining the grid inductance, its influence on the system stability is evaluated

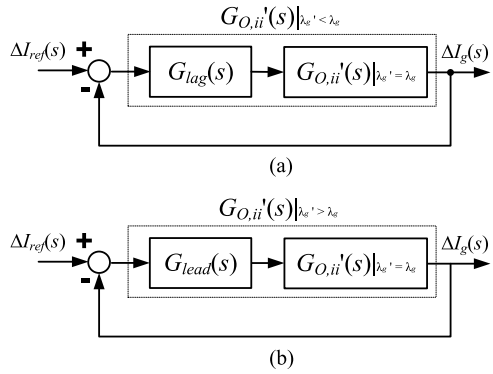

Fig. 13. Equivalent control block diagram for the grid inductance estimation. (a) When the estimation deviation is negative. (b) When the estimation deviation is positive.

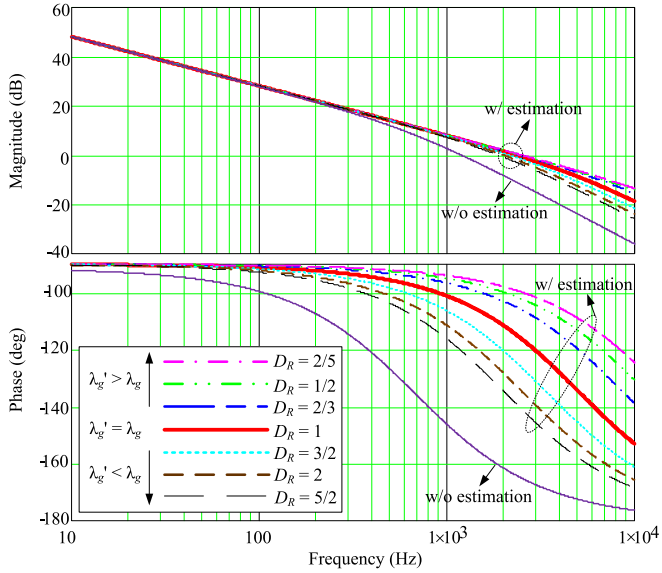

Fig. 14. Frequency plots of $G_{O,ii}(s)$ under different grid inductance estimation deviation ($L_g = 0.10$ p.u.).

below. Based on (36), the values of $G_{O,ii}(s)$ with $\lambda_g' \neq \lambda_g$ and $\lambda_g' = \lambda_g$ are compared under the worst case condition with $\alpha = \gamma = -0.2$ and $\beta = +0.2$ as follows:

$$G_L(s) = \frac{G_{O,ii}'(s)\big|_{\lambda_g' \neq \lambda_g}}{G_{O,ii}'(s)\big|_{\lambda_g' = \lambda_g}} = \frac{s+\frac{8}{3T_s}}{s\left(\frac{1+\lambda_g}{1+\lambda_g'}\right)+\frac{8}{3T_s}}$$
$$= \frac{s+\frac{8}{3T_s}}{sD_R+\frac{8}{3T_s}} \tag{37}$$

where D_R is defined as the deviation ratio.

$G_L(s)$ behaves as a lag compensator $G_{\text{Lag}}(s)$ when $\lambda_g' < \lambda_g$, and as a lead compensator $G_{\text{Lead}}(s)$ when $\lambda_g' > \lambda_g$ for $G_{O,ii}(s)$. Based on that, the equivalent control block diagrams for the grid inductance estimation with deviation are given in Fig. 13(a) and (b). When the deviation of the grid inductance estimation is negative, $G_{\text{Lag}}(s)$ reduces the system phase margin. Conversely, when the deviation of the grid inductance estimation is positive, $G_{\text{Lead}}(s)$ enhances the phase margin. However, the advantage is offset by the drawback of magnifying

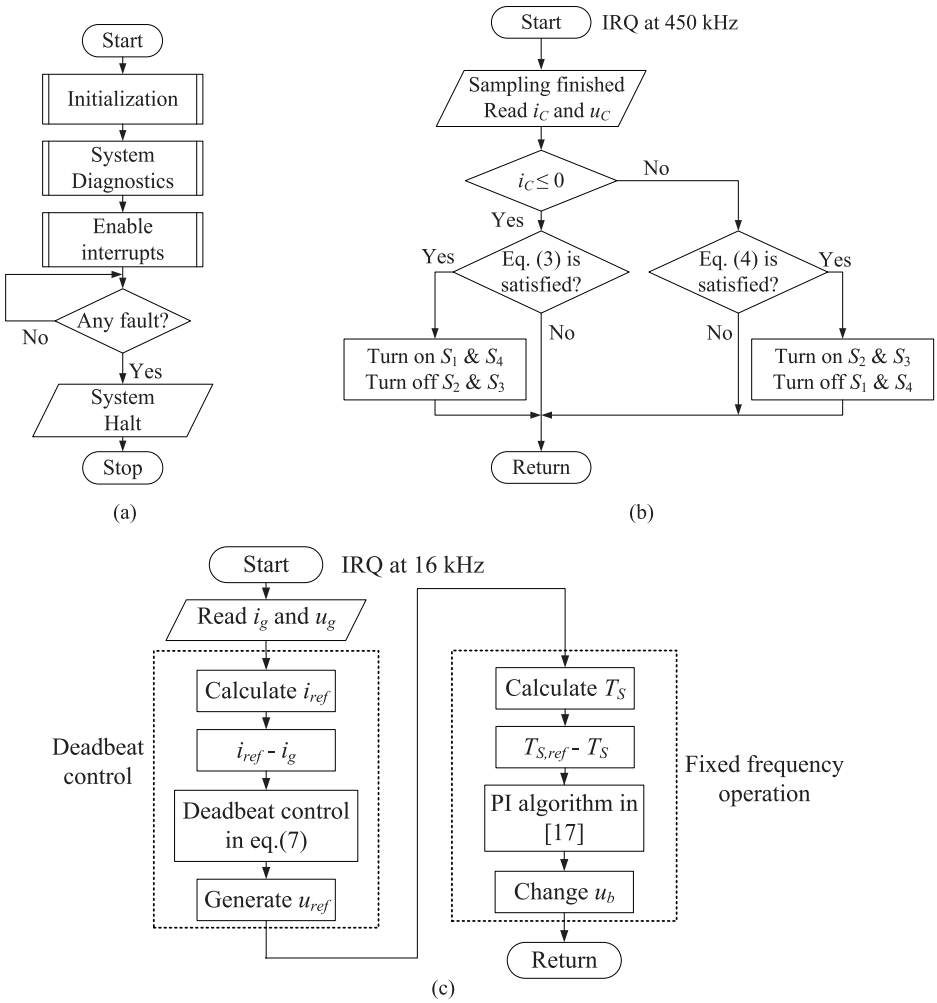

Fig. 15. Software flowchart. (a) Main program. (b) Interrupt service routine for the boundary control. (c) Interrupt service routine for the deadbeat control.

the noise level. A comparison of the system frequency response versus different deviations is shown in Fig. 14.

V. Experimental Verifications

A 2-kW, 220-V, 50-Hz inverter prototype has been built and evaluated. The design parameters are given in Table I. The prototype is supplied by a dc power supply EA-PSI 8500-30. The dc link voltage contains 100-Hz ripple. The peak-to-peak value of the ac ripple on the dc link is found to be 10% of the dc value. The inverter is controlled by using the digital controller TMS320F2808. The switching network is in BPWM and the dead time of the switching network is 1 μs.

The measured variables are i_C, i_g, u_C, u_g, and u_i. In principle, i_C can be replaced by measuring i_1. However, the resolution of the switching-frequency component of i_C is higher than that of i_1 practically, as i_C consists of much smaller line-frequency component than i_1. The sampling frequency for capacitor current i_C and filter capacitor voltage u_C is 450 kHz while the sampling frequency for grid current i_g, terminal voltage u_g and dc link voltage u_i is 16 kHz. The flowchart of the main program implemented on the digital controller is given in Fig. 15(a)–(c). Although i_C and u_C are sampled with a very high sampling rate, severe switching noises in the sampled signals are avoided as the switching always occurs after the sampling process as illustrated in Fig. 15(b).

A. Steady-State Performance

The steady-state characteristics of the system is investigated with $L_g = 0.0013$ p.u. (0.1 mH, stiff grid condition) and $L_g = 0.10$ p.u. (7.7 mH, weak-grid condition), respectively. Fig. 16 shows the steady-state waveforms of current injected into the PCC. With $L_g = 0.0013$ p.u., the total-harmonic-distortion (THD) of the terminal voltage and the injected current are 1.9% and 1.0%, respectively. With $L_g = 0.10$ p.u., the THD of the terminal voltage and the injected current are 2.0% and 0.9%, respectively. The results are measured by the digital power meter EVERFINE PF9811.

B. Transient Performance

The transient performance of the inverter is investigated under different grid inductances, when the grid current reference is suddenly changed from 4.6 to 9.1 A (i.e., from half power to

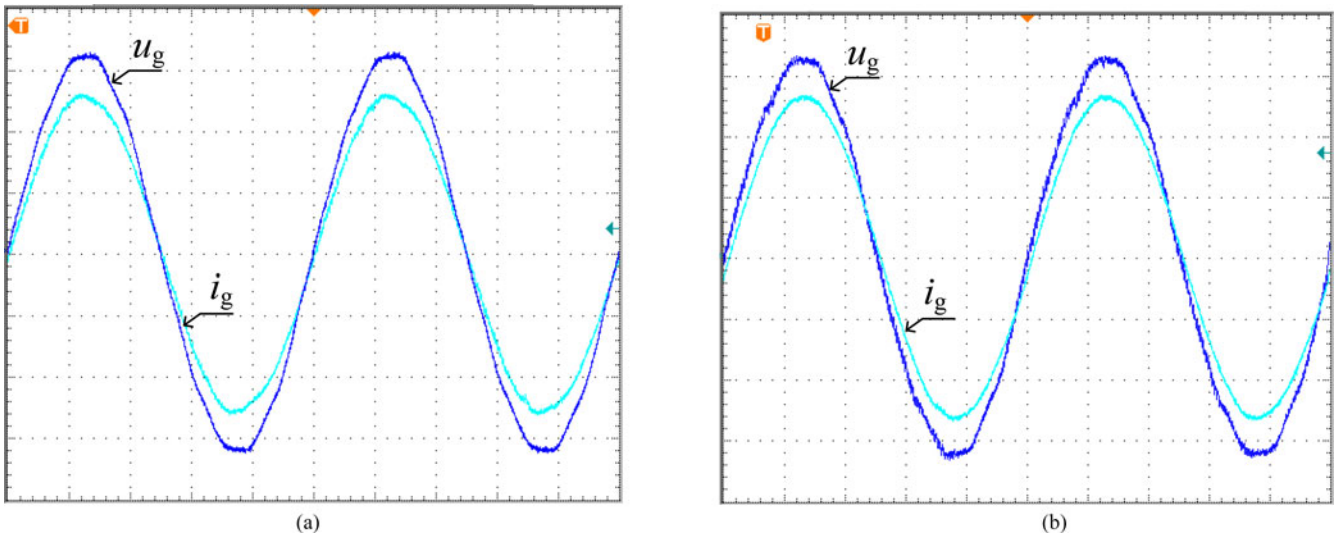

Fig. 16. Steady-state waveforms (u_g : 100 V/div, i_g : 5 A/div, and timebase: 4 ms/div). (a) $L_g = 0.0013$ p.u. (b) $L_g = 0.10$ p.u.

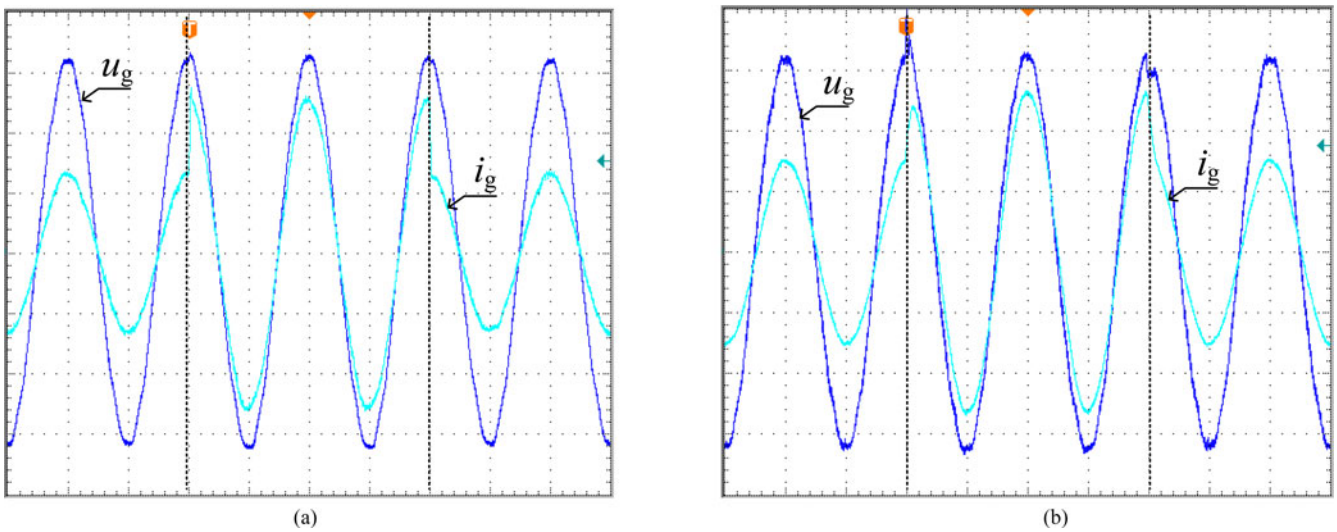

Fig. 17. Transient response (u_g : 100 V/div, i_g : 5 A/div, and timebase: 10 ms/div). (a) $L_g = 0.0013$ p.u. (b) $L_g = 0.10$ p.u.

full power), and *vice versa*. The corresponding experimental waveforms are shown in Fig. 17. Results reveal that the response time with the proposed control is shorter than 1 ms.

C. Harmonic Rejection Capability

To investigate the harmonic rejection capability of the system and the effectiveness of grid inductance estimation algorithm, a 1-kW nonlinear load is shunted at the PCC. The setup is shown in Fig. 18. The nonlinear load is a simple diode-capacitor rectifying circuit with an input filter inductor. Fig. 19 shows the measured %THD of the injected current i_g and terminal voltage u_g under different grid conditions with and without grid inductance estimation algorithm. Without the estimation algorithm, the % THD of the terminal voltage is 17.3% and that of the injected current is 6.3% under extremely weak grid condition with $L_g = 0.10$ p.u. (7.7 mH, worst-case condition).

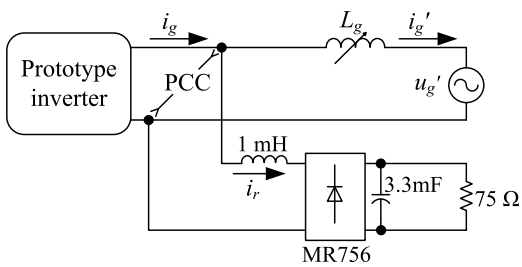

Fig. 18. Nonlinear load connected at the PCC.

With the grid inductance estimation algorithm, the %THD of the terminal voltage is 16.1% and that of the injected current is 5.2%.

Fig. 20 shows the harmonic spectra of the terminal voltage and injected current with $L_g = 0.10$ p.u. (7.7 mH, worst-case

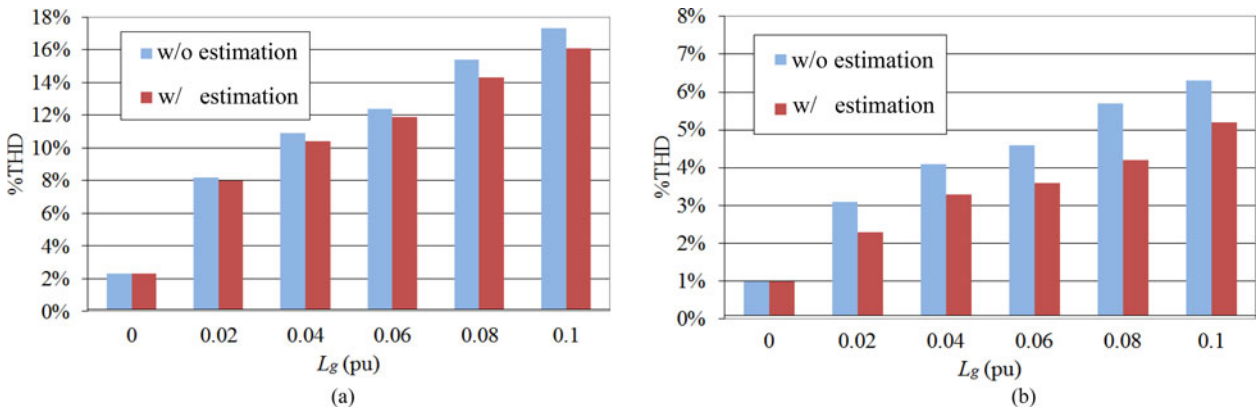

Fig. 19. Comparison of the %THD with and without the grid inductance estimation algorithm. (a) Terminal voltage. (b) Injected current.

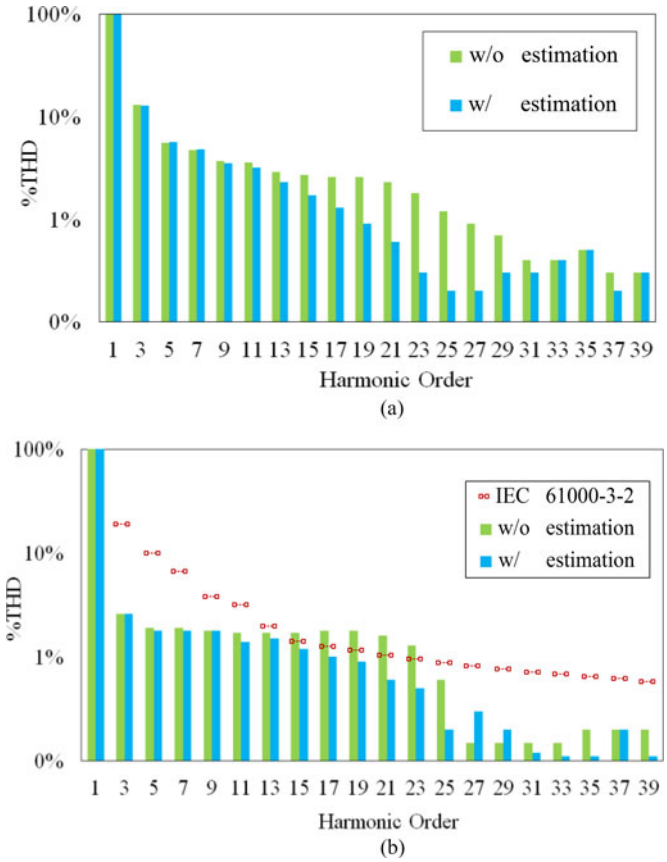

Fig. 20. Harmonic spectra of the terminal voltage and injected current with $L_g = 0.10$ p.u. (a) Terminal voltage. (b) Injected current.

condition). It indicates, even with highly-distorted terminal voltage, the injected current quality is guaranteed. The spectrum of the injected current is also compared with the limit of the IEC 61000-3-2 [33]. Even if the nonlinear load is connected to the PCC, the injected current still meets the standard requirement with the grid inductance estimation algorithm. Fig. 21(a) and (b) shows the waveforms of u_g, i_g, and i_r, where the voltage at the PCC is highly distorted due to the large grid inductance and the nonlinear current. Nevertheless, with the grid inductance estimation algorithm, the voltage at PCC will be less distorted with better quality injected current compared with that without the estimation algorithm.

Based on the experimental results, the proposed system with hybridized boundary and deadbeat control offers good harmonic rejection under both the stiff- and weak-grid condition. Furthermore, with the grid inductance estimation algorithm, the harmonic rejection capability can be significantly improved under the extremely weak grid.

VI. Conclusion

A hybridized architecture using a boundary control with second-order switching surface to reduce the order of the plant viewed by the deadbeat controller has been proposed. Such phenomenon would lay a foundation for the future research. Importantly, the parameters used in the control law are well defined and determined by the filter parameters. The performance sensitivities to filter parameters and grid inductance variations have been studied with the derived models. The proposed architecture guarantees wide control bandwidth and good grid disturbance rejection capability under both stiff- and weak-grid conditions. Together with a simple online grid inductance estimation algorithm, the control performance even with significant filter parameters drift is maintained in the extremely weak grid. The control architecture has been demonstrated on a 2-kW, 220-V, 50-Hz prototype to verify its validity. Even though the terminal voltage ($\%\text{THD} = 16.1\%$) is seriously distorted by a nonlinear load being shunt at the PCC of the extremely weak grid, the %THD of the injected current is only 5.2%.

Appendix

A. Derivations of (3) and (4)

The state-space equation in (2) is rewritten as

$$\begin{cases} \dfrac{di_C}{dt} \cong \dfrac{qu_i - u_C - [r_1 i_g + (r_1 + r_f) i_C]}{L_1} \\ i_C = C_f \dfrac{du_C}{dt}. \end{cases} \tag{A1}$$

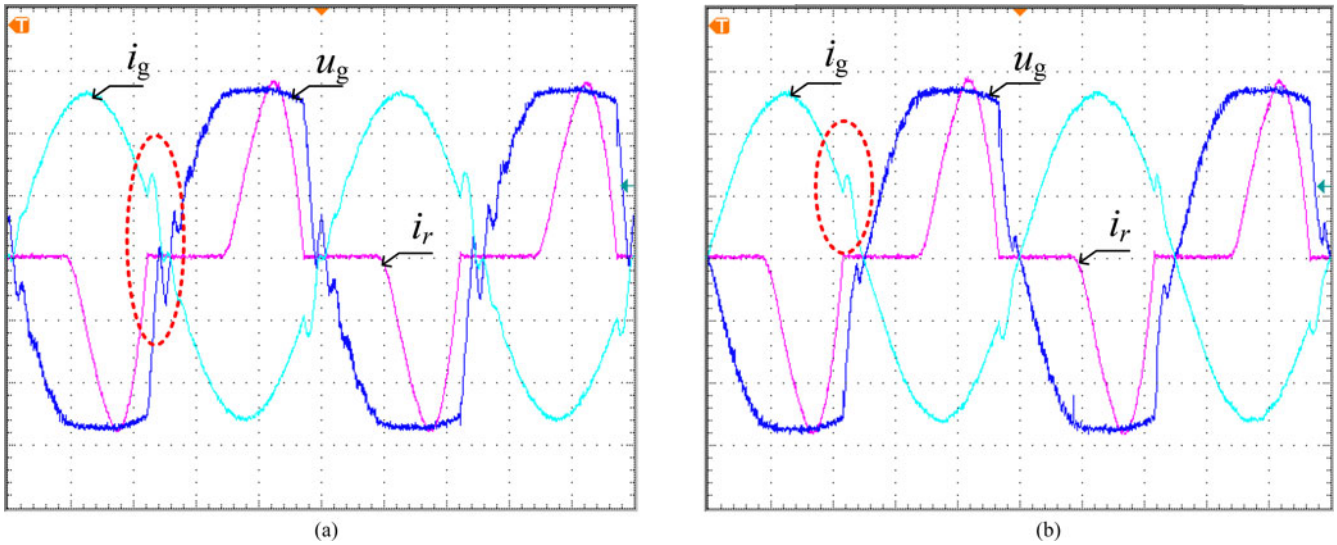

Fig. 21. Experimental waveforms with nonlinear load connected and $L_g = 0.10$ p.u. (u_g : 100 V/div, i_g : 5 A/div, and i_r : 5 A/div, and timebase: 4 ms/div). (a) Without grid inductance estimation. (b) With grid inductance estimation.

Considering that $|qu_i - u_C| >> |[r_1 i_g + (r_1 + r_f) i_C]|$, (A1) is simplified into

$$\begin{cases} \dfrac{di_C}{dt} \cong \dfrac{qu_i - u_C}{L_1} \\ i_C = C_f \dfrac{du_C}{dt}. \end{cases} \tag{A2}$$

(A2) can be rewritten as

$$\begin{cases} di_C = \dfrac{qu_i}{L_1} dt - \dfrac{u_C}{L_1} dt \\ \dfrac{1}{C_f} i_C = \dfrac{du_C}{dt}. \end{cases} \tag{A3}$$

Multiply the two equations in (A3) and integrate them

$$\frac{1}{C_f} \int i_C di_C = \frac{qu_i}{L_1} \int du_C - \frac{1}{L_1} \int u_C du_C. \tag{A4}$$

Fig. 22 shows the switching waveforms of u_C and i_C. Based on Fig. 22, solving the above integral equation from t_1 to t_2 in the Mode-1 operation, one can get

$$u_C(t_2) - u_C(t_1) = K_1(t_1) \left[i_C^2(t_2) - i_C^2(t_1) \right] \tag{A5}$$

where $K_1(t_1) = \frac{L_1}{2C_f[u_i - u_C(t_1)]}$.

Similarly, for the Mode-2 operation

$$u_C(t_4) - u_C(t_3) = K_2(t_3) \left[i_C^2(t_4) - i_C^2(t_3) \right] \tag{A6}$$

where $K_2(t_3) = \frac{-L_1}{2C_f[u_i + u_C(t_3)]}$.

By following Fig. 22 and substituting $u_C(t_2) = u_{C,\min}$ and $i_C(t_2) = I_{C,line}$ into (A5), the switching criterion for Mode 1 is

$$u_C(t) \le u_{C,\min}(t) + K_1(t) \left[i_C^2(t) - I_{C,line}^2(t) \right]. \tag{3}$$

By substituting $u_C(t_4) = u_{C,\max}$ and $i_C(t_4) = I_{C,line}$ into (A6), the switching criterion for Mode 2 is

$$u_C(t) \ge u_{C,\max}(t) + K_2(t) \left[i_C^2(t) - I_{C,\text{line}}^2(t) \right]. \tag{4}$$

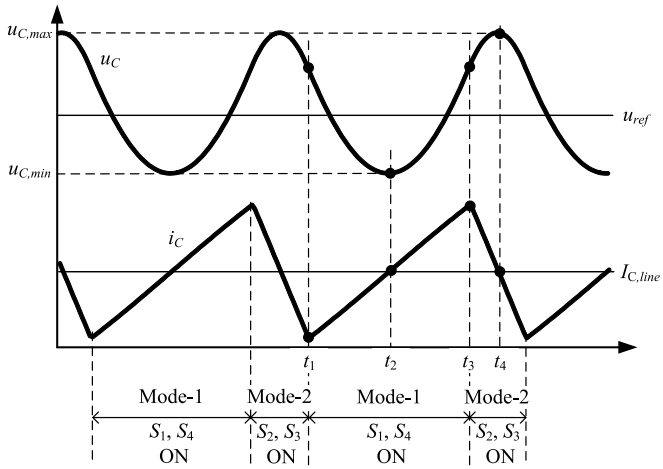

Fig. 22. Switching waveforms of u_C and i_C.

B. Derivations of (12)–(15)

Based on [22], the conditions leading to rejective mode are given by

$$\begin{cases} \sigma^{2}_{\Delta+}\big|_{\mathrm{M1}} < 0 \text{ or } \sigma^{2}_{\Delta-}\big|_{\mathrm{M1}} < 0, \dot{\sigma}^{2}_{\Delta+}\big|_{\mathrm{M1}} < 0 \\ \sigma^{2}_{\Delta+}\big|_{\mathrm{M2}} > 0 \text{ or } \sigma^{2}_{\Delta-}\big|_{\mathrm{M2}} > 0, \dot{\sigma}^{2}_{\Delta-}\big|_{\mathrm{M2}} > 0 \end{cases} \tag{A7}$$

and the ones ensuring reflective mode are

$$\begin{cases} \sigma^{2}_{\Delta+}\big|_{\mathrm{M1}} < 0 \text{ or } \sigma^{2}_{\Delta-}\big|_{\mathrm{M1}} < 0, \dot{\sigma}^{2}_{\Delta+}\big|_{\mathrm{M1}} > 0 \\ \sigma^{2}_{\Delta+}\big|_{\mathrm{M2}} > 0 \text{ or } \sigma^{2}_{\Delta-}\big|_{\mathrm{M2}} > 0, \dot{\sigma}^{2}_{\Delta-}\big|_{\mathrm{M2}} < 0 \end{cases} \tag{A8}$$

where M1 and M2 means the corresponding value at Mode-1 state and Mode-2 state, respectively. $\dot{\sigma}^{2}_{\Delta+}\big|_{\mathrm{M1}}$ is the change rate of $\sigma^{2}_{\Delta+}\big|_{\mathrm{M1}}$ at Mode-1 state while $\dot{\sigma}^{2}_{\Delta-}\big|_{\mathrm{M2}}$ is the one of $\sigma^{2}_{\Delta-}\big|_{\mathrm{M2}}$ at Mode-2 state. By substituting (9)–(10) to (11), it

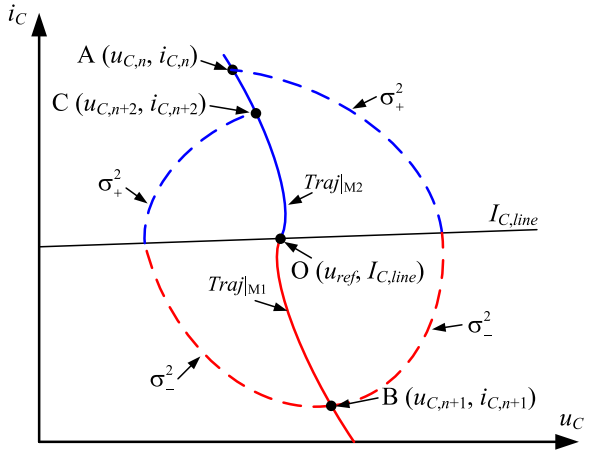

Fig. 23. Illustration of the successor point movement in refractive mode.

has

$$\sigma\,{}^{2}_{\Delta+}\big|_{\mathrm{M1}} = 2[K_{S1}(t) - K_2(t)]i_C^2(t) \tag{A9a}$$

$$\sigma\,{}^{2}_{\Delta-}\big|_{\mathrm{M1}} = 2[K_{S1}(t) - K_1(t)]i_C^2(t) \tag{A9b}$$

$$\sigma\,{}^{2}_{\Delta+}\big|_{\mathrm{M1}} = 2[K_{S1}(t) - K_2(t)]i_C(t)\,\frac{d}{dt}i_C(t)\Big|_{\mathrm{M1}} \quad (i_C(t) > 0) \tag{A9c}$$

and

$$\sigma\,{}^{2}_{\Delta+}\big|_{\mathrm{M2}} = 2[K_{S2}(t) - K_2(t)]i_C^2(t) \tag{A10a}$$

$$\sigma\,{}^{2}_{\Delta-}\big|_{\mathrm{M2}} = 2[K_{S2}(t) - K_1(t)]i_C^2(t) \tag{A10b}$$

$$\sigma^2_{\Delta-}\Big|_{\mathrm{M2}} = 2[K_{S2}(t) - K_1(t)]i_C(t)\,\frac{d}{dt}i_C(t)\Big|_{\mathrm{M2}} \quad (i_C(t) < 0). \tag{A10c}$$

By combining (A7)–(A10), the regions of the control parameters for rejective and reflective modes are

$$K_1(t) < K_{S2}(t) \text{ and } K_2(t) > K_{S1}(t) \tag{12}$$

$$K_1(t) > K_{S1}(t) \text{ and } K_2(t) < K_{S2}(t) \tag{13}$$

and the regions of the control parameters for refractive mode, that is outside rejective and reflective modes, are

$$K_{S2}(t) < K_1(t) < K_{S1}(t) \text{ or} \tag{14a}$$

$$K_1(t) > K_{S1}(t) \text{ and } K_2(t) > K_{S2}(t) \text{ or} \tag{14b}$$

$$K_1(t) < K_{S2}(t) \text{ and } K_2(t) < K_{S1}(t). \tag{14c}$$

In refractive mode, the stability is assured only if each successive intersection with the switch surface drives the operation closer to the target point "O" as shown in Fig. 23. For example, in Fig. 23, "A" ($u_{C,n}$,$i_{C,n}$), "B" ($u_{C,n+1}$,$i_{C,n+1}$), and "C" ($u_{C,n+2}$,$i_{C,n+2}$) are three subsequent successive intersections between the state trajectories in (9) and (10) and the switching surface in (11). The condition for stable operation is

$$S_{n+2} < S_n \tag{A11}$$

where S_n is the distance between the successive point "A" and the target point "O" (u_{ref},$I_{C,\mathrm{line}}$), $S_n^2 = (u_{C,n} - u_{\mathrm{ref}})^2 + (i_{C,n} - I_{C,\mathrm{line}})^2$. Similarly, S_{n+2} is the distance between "C" and "O," $S_{n+2}^2 = (u_{C,n+2} - u_{\mathrm{ref}})^2 + (i_{C,n+2} - I_{C,\mathrm{line}})^2$. By neglecting the hysteresis band $u_b(t)$ in (11)

$$\begin{cases} u_{C,n} - u_{\mathrm{ref}} = K_1\left[i_{C,n}^2 - I_{C,\mathrm{line}}^2\right] \\ u_{C,n+2} - u_{\mathrm{ref}} = K_1\left[i_{C,n+2}^2 - I_{C,\mathrm{line}}^2\right]. \end{cases} \tag{A12}$$

Thus, the condition in (A11) is simplified as

$$|i_{C,n+2}| < |i_{C,n}|. \tag{A13}$$

In Fig. 23, the successor points "A" and "C" are on σ_+^2 and "B" is on σ_-^2 as given in (11). Similarly, both "A" and "B" are on the $\mathrm{Traj}|_{\mathrm{M_2}}$ while both "B" and "C" are on the $\mathrm{Traj}|_{\mathrm{M_1}}$ as presented in (9) and (10). Based on (9)–(11), it can be shown that

$$i_{C,n+2}^2 = i_{C,n}^2 \frac{K_{S1} - K_1}{K_{S1} - K_2}\frac{K_{S2} - K_2}{K_{S2} - K_1}. \tag{A14}$$

By substituting (A14) into (A13) and combining it with (14), the condition for stable operation in refractive mode is obtained as

$$K_1(t) > K_2(t). \tag{15}$$

C. Derivation of (21)

Consider the Mode-1 operation. Let t_1 have the dc value of T_1 and small-signal perturbation of Δt_1

$$t_1 = T_1 + \Delta t_1. \tag{16}$$

u_C, $u_{C,\min}$, and i_C are expressed as

$$u_C(t_1) = U_C(T_1) + \Delta u_C(t_1) \tag{A16}$$

$$u_{C,\min}(t_1) = U_{C,\min}(T_1) + \Delta u_{C,\min}(t_1) \tag{A17}$$

$$i_C(t_1) = I_C(T_1) + \Delta i_C(t_1) \tag{A18}$$

where $U_C(T_1)$, $U_{C,\min}(T_1)$, and $I_C(T_1)$ are the dc values of u_C, $u_{C,\min}$, and i_C, respectively, and $\Delta u_C(t_1)$, $\Delta u_{C,\min}(t_1)$, and $\Delta i_C(t_1)$ are the small-signal perturbations of u_C, $u_{C,\min}$, and i_C, respectively.

Then, by substituting (A16)–(A18) into (17), the dc equation is

$$U_C(T_1)[U_{\mathrm{in}} - U_C(T_1)] = U_{C,\min}(T_1)[U_{\mathrm{in}} - U_C(T_1)] + \frac{L_{1,N}}{2C_{f,N}}[I_C^2(T_1) - I_{C,\mathrm{line}}^2]. \tag{A19}$$

By neglecting the higher-order terms, the linearized ac equation is

$$[U_{\mathrm{in}} - 2U_C(T_1) + U_{C,\min}(T_1)]\,\Delta u_C(t_1) = [U_{\mathrm{in}} - U_C(T_1)]\,\Delta u_{C,\min}(t_1) + \frac{L_{1,N}\,[I_C(T_1) - I_{C,\mathrm{line}}]}{C_{f,N}}\Delta i_C(t_1). \tag{A20}$$

At the steady state

$$U_C(T_1) \cong U_{C,\min}(T_1) \tag{A21}$$

and

$$I_C(T_1) - I_{C,\text{line}} = -\frac{\Delta I_1}{2} = -\frac{[U_{\text{in}} - U_C(T_1)]}{2L_{1,N}(1+\alpha)} D\, T_S \quad \text{(A22)}$$

where $D = (t_3 - t_1) / T_S$ is the duty ratio of Mode 1, and T_S is switching period.

The variation of the filter-capacitor current is

$$\Delta i_C(t_1) = C_{f,N}(1+\beta)\frac{d}{dt}\Delta u_C(t_1). \quad \text{(A23)}$$

Substitute (A21)–(A23) into (A20)

$$\Delta u_{C,\min}(t_1) = \frac{D\, T_S\, (1+\beta)}{2\,(1+\alpha)}\frac{d}{dt}\Delta u_C(t_1) + \Delta u_C(t_1). \quad \text{(A24)}$$

Similarly, by following equation can be derived for the Mode-2 operation

$$\Delta u_{C,\max}(t_3) = \frac{(1-D)\, T_S (1+\beta)}{2\,(1+\alpha)}\frac{d}{dt}\Delta u_C(t_3) + \Delta u_C(t_3). \quad \text{(A25)}$$

Based on (13) and (14)

$$\Delta u_{C,\min}(t_1) = \Delta u_{\text{ref}}(t_1) - \Delta u_b(t_1) \quad \text{(A26)}$$

$$\Delta u_{C,\max}(t_3) = \Delta u_{\text{ref}}(t_3) + \Delta u_b(t_3). \quad \text{(A27)}$$

In order to study the low-frequency characteristics, the following assumptions are made:

$$\Delta u_C(t_1) \cong \Delta u_C(t_3) \quad \text{(A28)}$$

$$\Delta u_{\text{ref}}(t_1) \cong \Delta u_{\text{ref}}(t_3) \quad \text{(A29)}$$

$$\Delta u_b(t_1) \cong \Delta u_b(t_3). \quad \text{(A30)}$$

By substituting (A20)–(A22) into (A16)–(A19)

$$\Delta u_{\text{ref}}(t) = \frac{T_S\,(1+\beta)}{4(1+\alpha)}\,\frac{d}{dt}\,\Delta u_C(t) + \Delta u_C(t). \quad \text{(A29)}$$

Thus, the closed-loop transfer function of the second-order switching surface-based boundary control, $G_{BC}(s)$, is obtained by performing Laplace transformation of (A31).

$$G_{BC}(s) = \frac{\Delta U_C(s)}{\Delta U_{\text{ref}}(s)} = \frac{1}{s\frac{T_S(1+\beta)}{4(1+\alpha)} + 1}. \quad \text{(21)}$$

REFERENCES

[1] Y. Xue, L. Chang, S. B. Kjaer, J. Bordoau, and T. Shimizu, "Topologies of single phase inverters for small distributed power generators: An overview," *IEEE Trans. Power Electron.*, vol. 19, no. 5, pp. 1305–1314, Sep. 2004.

[2] F. Blaabjerg, R. Teodorescu, M. Liserre, and A. V. Timbus, "Overview of control and grid synchronization for distributed power generation systems," *IEEE Trans. Ind. Electron.*, vol. 53, no. 5, pp. 1398–1409, Oct. 2006.

[3] M. Lindgren and J. Svensson, "Control of a voltage-source converter connected to the grid through an LCL-filter-application to active filtering," in *Proc. IEEE Power Electron. Spec. Conf.*, May 1998, pp. 229–235.

[4] T. G. Habetler, "A space vector-based rectifier regulator for AC/DC/AC converters," *IEEE Trans. Power Electron.*, vol. 8, no. 1, pp. 30–36, Jan. 1993.

[5] D. G. Holmes and D. A. Martin, "Implementation of a direct digital predictive current controller for single and three phase voltage source inverters," in *Proc. IEEE Ind. Appl. Conf.*, Oct. 1996, pp. 906–913.

[6] J. He, Y. W. Li, D. Bosnjak, and B. Harris, "Investigation and active damping of multiple resonances in a parallel-inverter-based microgrid," *IEEE Trans. Power Electron.*, vol. 28, no. 1, pp. 234–246, Jan. 2013.

[7] E. Wu and P. W. Lehn, "Digital current control of a voltage source converter with active damping of LCL resonance," *IEEE Trans. Power Electron.*, vol. 21, no. 5, pp. 1364–1373, Sep. 2006.

[8] Y. A. I. Mohamed, "Suppression of low- and high-frequency instabilities and grid-induced disturbances in distributed generation inverters," *IEEE Trans. Power Electron.*, vol. 26, no. 12, pp. 3790–3803, Dec. 2011.

[9] S. G. Parker, B. P. McGrath, and D. G. Holmes, "Regions of active damping control for LCL filters," *IEEE Trans. Ind. Appl.*, vol. 50, no. 1, pp. 424–432, Jan./Feb. 2014.

[10] C. Bao, X. Ruan, X. Wang, W. Li, D. Pan, and K. Weng, "Step-by-step controller design for LCL-type grid-connected inverter with capacitor-current-feedback active-damping," *IEEE Trans. Power Electron.*, vol. 29, no. 3, pp. 1239–1253, Mar. 2014.

[11] D. Pan, X. Ruan, C. Bao, W. Li, and X. Wang, "Capacitor-current-feedback active damping with reduced computation delay for improving robustness of LCL-type grid-connected inverter," *IEEE Trans. Power Electron.*, vol. 29, no. 7, pp. 3414–3427, Jul. 2014.

[12] D. Yang, X. Ruan, and H. Wu, "A real-time computation method with dual sampling modes to improve the current control performances of the LCL-type grid-connected inverter," *IEEE Trans. Ind. Electron.*, vol. 62, no. 7, pp. 4563–4572, Jul. 2015.

[13] L. Corradini, P. Mattavelli, and S. Saggini, "Elimination of sampling-induced dead bands in multiple-sampled pulsewidth modulators for DC–DC converters," *IEEE Trans. Power Electron.*, vol. 24, no. 11, pp. 2661–2665, Aug. 2009.

[14] V. Miskovic, V. Blasko, T. Jahns, A. Smith, and C. Romenesko, "Observer based active damping of LCL resonance in grid connected voltage source converters," *IEEE Trans. Ind. Appl.*, vol. 50, no. 6, pp. 3977–3985, Nov./Dec. 2014.

[15] K. Leung and H. Chung, "Derivation of a second-order switching surface in the boundary control of buck converters," *IEEE Power Electron. Lett.*, vol. 2, no. 2, pp. 63–67, Jun. 2004.

[16] K. W. Chan, H. Chung, and S. Y. Hui, "A generalized theory of boundary control for a single-phase multilevel inverter using second-order switching surface," *IEEE Trans. Power Electron.*, vol. 24, no. 10, pp. 2298–2313, Oct. 2009.

[17] W. T. Yan, C. Ho, and H. Chung, "Fixed-frequency boundary control of buck converter with second-order switching surface," *IEEE Trans. Power Electron.*, vol. 24, no. 9, pp. 2193–2201, Sep. 2009.

[18] L. Malesani, P. Mattavelli, and S. Buso, "Robust dead-beat current control for PWM rectifiers and active filters," *IEEE Trans. Ind. Appl.*, vol. 35, no. 3, pp. 613–620, May/Jun. 1999.

[19] K. Leung and H. Chung, "A comparative study of the boundary control of buck converters using first- and second-order switching surfaces," *IEEE Trans. Power Electron.*, vol. 22, no. 4, pp. 1196–1209, Jul. 2007.

[20] M. Ordonez, J. E. Quaicoe, and M. T. Iqbal, "Advanced boundary control of inverters using the natural switching surface: Normalized geometrical derivation," *IEEE Trans. Power Electron.*, vol. 23, no. 6, pp. 2915–2930, Nov. 2008.

[21] G. Feng, E. Meyer, and Y.-F. Liu, "A new digital control algorithm to achieve optimal dynamic performance in dc-to-dc converters," *IEEE Trans. Power Electron.*, vol. 22, no. 4, pp. 1489–1498, Jul. 2007.

[22] C. N. Ho and H. S. Chung, "Implementation and performance evaluation of a fast dynamic control scheme for capacitor-supported interline DVR," *IEEE Trans. Power Electron.*, vol. 25, no. 8, pp. 1975–1988, Aug. 2010.

[23] P. T. Krein, *Nonlinear Phenomena in Power Electronics: Attractors, Bifurcation, Chaos, and Nonlinear Control*. New York, NY, USA: IEEE Press, 2001.

[24] R. B. Ridley, B. H. Cho, and F. C. Y. Lee, "Analysis and implementation of loop gains of multiloop-controlled switching regulators," *IEEE Trans. Power Electron.*, vol. 3, no. 4, pp. 489–498, Oct. 1988.

[25] T. Abeyasekera, C. M. Johnson, D. J. Atkinson, and M. Armstrong, "Suppression of line voltage related distortion in current controlled grid connected inverters," *IEEE Trans. Power Electron.*, vol. 20, no. 6, pp. 1393–1401, Nov. 2005.

[26] J. Sun, "Impedance-based stability criterion for grid-connected inverters," *IEEE Trans. Power Electron.*, vol. 26, no. 11, pp. 3075–3078, Nov. 2011.

[27] S. Cobreces, E. J. Bueno, D. Pizarro, F. J. Rodriguez, and F. Huerta, "Grid impedance monitoring system for distributed power generation electronic interfaces," *IEEE Trans. Instrum. Meas.*, vol. 58, no. 9, pp. 3112–3121, Jun. 2009.
[28] N. Hoffmann and F. W. Fuchs, "Minimal invasive equivalent grid impedance estimation in inductive–resistive power networks using extended Kalman filter," *IEEE Trans. Power Electron.*, vol. 29, no. 2, pp. 631–641, Apr. 2013.
[29] G. Shen, J. Zhang, X. Li, C. Du, and D. Xu, "Current control optimization for grid-tied inverters with grid impedance estimation," in *Proc. IEEE Appl. Power Electron. Conf.*, Feb. 2010, pp. 861–866.
[30] L. Asiminoaei, R. Teodorescu, F. Blaabjerg, and U. Borup, "Implementation and test of an online embedded grid impedance estimation technique for PV inverters," *IEEE Trans. Ind. Electron.*, vol. 52, no. 4, pp. 1136–1144, Aug. 2005.
[31] T. Roinila, M. Vilkko, and J. Sun, "Online grid impedance measurement using discrete-interval binary sequence injection," in *Proc. IEEE Control Modeling Power Electron.*, Jun. 2013, pp. 1–8.
[32] M. Liserre, F. Blaabjerg, and R. Teodorescu, "Grid impedance estimation via excitation of LCL-filter resonance," *IEEE Trans. Ind. Appl.*, vol. 43, no. 5, pp. 1401–1407, Sep./Oct. 2007.
[33] *Electromagnetic Compatibility (EMC)—Part 3-2: Limits—Limits for Harmonic Current Emissions (Equipment Input Current $<=$ 16 A per Phase)*, IEC 61000-3-2: 2005+A1:2008+A2:2009, 2005.

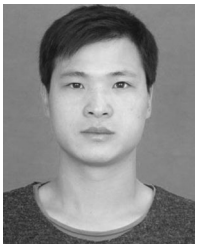

Yuanbin He (S'14) received the B.Eng. and M.Eng. degrees in electrical engineering, from Shanghai Maritime University, Shanghai, China, in 2009 and 2011, respectively. He is currently working toward the Ph.D. degree in power electronics at the City University of Hong Kong, Hong Kong.

He worked as an Associate Researcher at Nanjing FSP-Powerland Technology Technology Inc., Nanjing, China, until March 2013, where he had been engaged in research and development of dc–dc and dc–ac converters. His current research interests include digital control technique and renewable energy generation system.

Henry Shu-Hung Chung (M'95–SM'03) received the B.Eng. degree in 1991 and the Ph.D. degree, in 1994, in electrical engineering, both from the Hong Kong Polytechnic University, Hong Kong.

Since 1995, he has been with the City University of Hong Kong, Hong Kong. He is currently Professor of the Department of Electronics Engineering, and the Director of the Centre for Smart Energy Conversion and Utilization Research. His research interests include time- and frequency-domain analysis of power electronic circuits, switched-capacitor-based converters, random-switching techniques, control methods, digital audio amplifiers, soft-switching converters, and electronic ballast design. He has edited one book, and authored eight research book chapters, and more than 320 technical papers including 160 refereed journal papers in his research areas, and holds 32 patents.

Dr. Chung is currently Editor-in-Chief of the IEEE POWER ELECTRONICS LETTERS, and Associate Editor of the IEEE TRANSACTIONS ON POWER ELECTRONICS, and the IEEE JOURNAL OF EMERGING AND SELECTED TOPICS IN POWER ELECTRONICS.

Carl Ngai-Man Ho (M'07–SM'12) received the B.Eng. and M.Eng. double degrees and the Ph.D. degree in electronic engineering from the City University of Hong Kong, Hong Kong, in 2002 and 2007, respectively.

His Ph.D. research was focused on the development of dynamic voltage regulation and restoration technology. From 2002 to 2003, he was a Research Assistant at the City University of Hong Kong. From 2003 to 2005, he was an Engineer at e.Energy Technology Ltd., Hong Kong. In 2007, he joined ABB Switzerland. He has been appointed as Scientist, Principal Scientist, Global Intellectual Property Coordinator and the last position was R&D Principal Engineer. He has led a research project team at ABB for three years to develop solar inverter technologies. In October 2014, he joined the University of Manitoba, Winnipeg, MB, Canada, as Assistant Professor and Canada Research Chair in Efficient Utilization of Electric Power. He takes up the challenge of research into microgrid technologies, renewable energy interfaces and demand side control methodologies.

Dr. Ho is currently an Associate Editor of the IEEE TRANSACTIONS ON POWER ELECTRONICS and Guest Associate Editor of the IEEE JOURNAL OF EMERGING AND SELECTED TOPICS IN POWER ELECTRONICS - SPECIAL ISSUE ON SUSTAINABLE ENERGY SYSTEMS INTEGRATION.

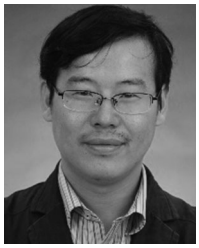

Weimin Wu received the Ph.D. degree from the College of Electrical Engineering, Zhejiang University, Hangzhou, China, in 2005.

He worked as a Research Engineer at the Delta Power Electronic Center, Shanghai, China, from July 2005 to June 2006. Since July 2006, he has been a faculty member at Shanghai Maritime University, Shanghai, where he is currently a Full Professor at the Department of Electrical Engineering. He was a Visiting Professor at the Center for Power Electronics Systems, Virginia Polytechnic Institute and State University, Blacksburg, from September 2008 to March 2009. From November 2011 to January 2014, he was also a Visiting Professor at the Department of Energy Technology, working at the Center of Reliable Power Electronics. He has coauthored more than 60 papers and holds six patents. His areas of interests include power converters for renewable energy systems, power quality, smart grid, and energy storage technology.